NANO · MICRO small
www.small-journal.com

Robust Biomass-Derived Carbon Frameworks as High-Performance Anodes in Potassium-Ion Batteries

Jintao Chen, Guanxu Chen,* Siyu Zhao,* Junrun Feng,* Ryan Wang,* Ivan P. Parkin,* and Guanjie He**

Potassium-ion batteries (PIBs) have become one of the promising candidates for electrochemical energy storage that can provide low-cost and high-performance advantages. The poor cyclability and rate capability of PIBs are due to the intensive structural change of electrode materials during battery operation. Carbon-based materials as anodes have been successfully commercialized in lithium- and sodium-ion batteries but is still struggling in potassium-ion battery field. This work conducts structural engineering strategy to induce anionic defects within the carbon structures to boost the kinetics of PIBs anodes. The carbon framework provides a strong and stable structure to accommodate the volume variation of materials during cycling, and the further phosphorus doping modification is shown to enhance the rate capability. This is found due to the change of the pore size distribution, electronic structures, and hence charge storage mechanism. The optimized electrode in this work shows a high capacity of 175 mAh g^{-1} at a current density of 0.2 A g^{-1} and the enhancement of rate performance as the PIB anode (60% capacity retention with the current density increase of 50 times). This work, therefore provides a rational design for guiding future research on carbon-based anodes for PIBs.

1. Introduction

In terms of clean, reliable, low-cost, and environmentally friendly energy storage solutions, lithium-ion batteries (LIBs) are facing challenges due to the shortage of lithium resources and increasing costs.[1] Energy consumption in the world is increasing dramatically in recent years, especially, the development of the internet accelerated the consumption substantially.[2,3] As one of the promising substitutional options for LIBs, potassium-ion batteries (PIBs) have been intensively studied in the research field of electrochemical energy storage. Sodium and potassium are much more earth abundant than lithium. Additionally, as potassium metal does not react with aluminium in the low potential range, it provides the possibility of substituting copper with aluminium as the current collector, which further reduces the cost of PIBs.[1] However, PIBs are still facing challenges including their slow kinetics, poor cyclability due to severe volume change during cycling, and the side reactions between electrodes and unmatched electrolytes.[4,5] The sluggish kinetics and substantial structural strain during cycling of PIBs is due to the large ionic radius of the potassium-ion.[6–12] To solve this issue, nanostructure design was attempted in many works on a wide range of materials, including graphite,[13,14] graphene oxides,[15] alloys,[16] sulfides,[17] selenides,[18,19] and Prussian blue analogues,[20] to shorten ion diffusion length of potassium (K^+) ions and increase the numbers of paths by changing the morphology and microstructure.

Carbon-based materials are important in K^+ ion batteries because of their excellent electrical conductivity, low voltage discharge plateaus, high theoretical specific capacity, and low cost. Carbon-based materials have been proved to be reliable anodes or essential electrode composition in the forms of graphene, carbon nanotubes (CNTs),[21–26] graphite,[27–33] graphene oxide (GO), or reduced graphene oxide (rGO).[15,17,18,34] Nevertheless, there are still many challenges in the utilization of carbon materials as anode in potassium ion batteries: 1) interlayer spacing is not sufficient in many carbon materials. Commercial graphite usually has a interlayer spacing of 0.335 nm to accommodate large K^+ ions (1.38 Å), which results in poor rate capability and fast capacity decay. 2) Severe volume variation during charge–discharge processes, which results in limited cycling stability; several structural engineering approaches have been studied for CNTs, including metal-organic framework.[35] 3) Costly method and byproduct produced in the synthesis also need to be considered when designing anodes.

J. Chen, I. P. Parkin, G. He
Department of Chemistry
University College London
20 Gordon Street, London WC1H 0AJ, UK
E-mail: jintao.chen.17@ucl.ac.uk; i.p.parkin@ucl.ac.uk; g.he@ucl.ac.uk
G. Chen, S. Zhao, J. Feng, R. Wang, G. He
Department of Chemical Engineering
University College London
London WC1E 7JE, UK
E-mail: g.chen.17@ucl.ac.uk; s.zhao.17@ucl.ac.uk; junrun.feng.17@ucl.ac.uk; ryan.wang@ucl.ac.uk

The ORCID identification number(s) for the author(s) of this article can be found under https://doi.org/10.1002/smll.202206588.

DOI: 10.1002/smll.202206588

Wang et al. have reported that the pure CNTs power as an anode exhibited low capacity (<100 mAh g^{-1}) and decay to zero after 300 cycles. The ex situ analysis pointed out that this is due to the structural collapse of fractured CNTs and the K^+ ion intercalation mainly takes place in loose layers from the outer-shell CNTs of the multiwalled carbon nanotubes (MWCNTs).

Structural engineering by heteroatom doping was carried out in this work by providing more active sites and ion exchange paths for ion transport. The rate performance, as well as the long cycle performance of the cell in this study, were also largely improved by the engineering design.[7,36–38] Additionally, this work highlights the impact of P doping and its results in pore size distribution, which can contribute to high-rate performance. The volume change, which is associated with severe safety issues and fast decay in the battery capacity, of layered graphitic anode materials in PIBs has been proved to be over 60% volume expansion after K^+ ion intercalation, which was six times higher than that in LIBs.[39]

Herein, a study of the carbon materials glucose combined with MWCNTs (GCNTs) and GCNTs with heteroatom phosphorous (P) (PGCNTs) doping was carried out to achieve high rate-performance by changing the electronic structure, pore distribution in carbon structure without sacrificing in capacity. The composites in this study were synthesized by one-step hydrothermal reaction followed by atom doping. Different from other carbon-based materials made by electrospinning, solution-based chemical methods, ball-milling, the synthesis process is low-cost and free of byproduct. Additionally, all the ingredients used in this work are commercialized in the market with relatively low cost. In this study, carbon-based materials in the composite can provide tremendous surface area and ion exchange pathway to achieve high capacity, whereas the glucose provides the CNTs with a carbon coating by $\pi - \pi$ bonds, which lead to the easy combination of CNTs with ions or functional groups and therefore provide the batteries with high cyclability (148 mAh g^{-1} at 950th cycle). The GCNTs were further modified by P doping to enhance their rate performance and change pore size distribution and kinetic behaviors. The doping effect was also optimized by different ratios of dopants, and it was confirmed that the doping can largely enhance the rate performance by five times (from 20 to 100 mAh g^{-1}) at 5 A g^{-1}.

2. Results and Discussion

Scanning electron microscope (SEM) was applied for morphology characterization to identify the porous structure after structural engineering by annealing. Annealing can also provide the composites with more active sites, increase surface area, and reduce oxygen functional groups. As is shown in **Figure 1**a,b, annealed pristine carbon nanotubes stacked together and combined with carbon, which can provide more active structures for K^+ ion intercalation/deintercalation and more tunnels for K^+ ion transfer, which can lead to better reaction kinetics. Additionally, it was found that the ratio of glucose is of vital importance. The excess glucose in the hydrothermal reaction leads to the carbon cluster in the product (Figure S1, Supporting Information), however, as is shown in Figure 1b, there is no obvious carbon cluster in the product, which can confirm that the PGCNT materials were not affected by the

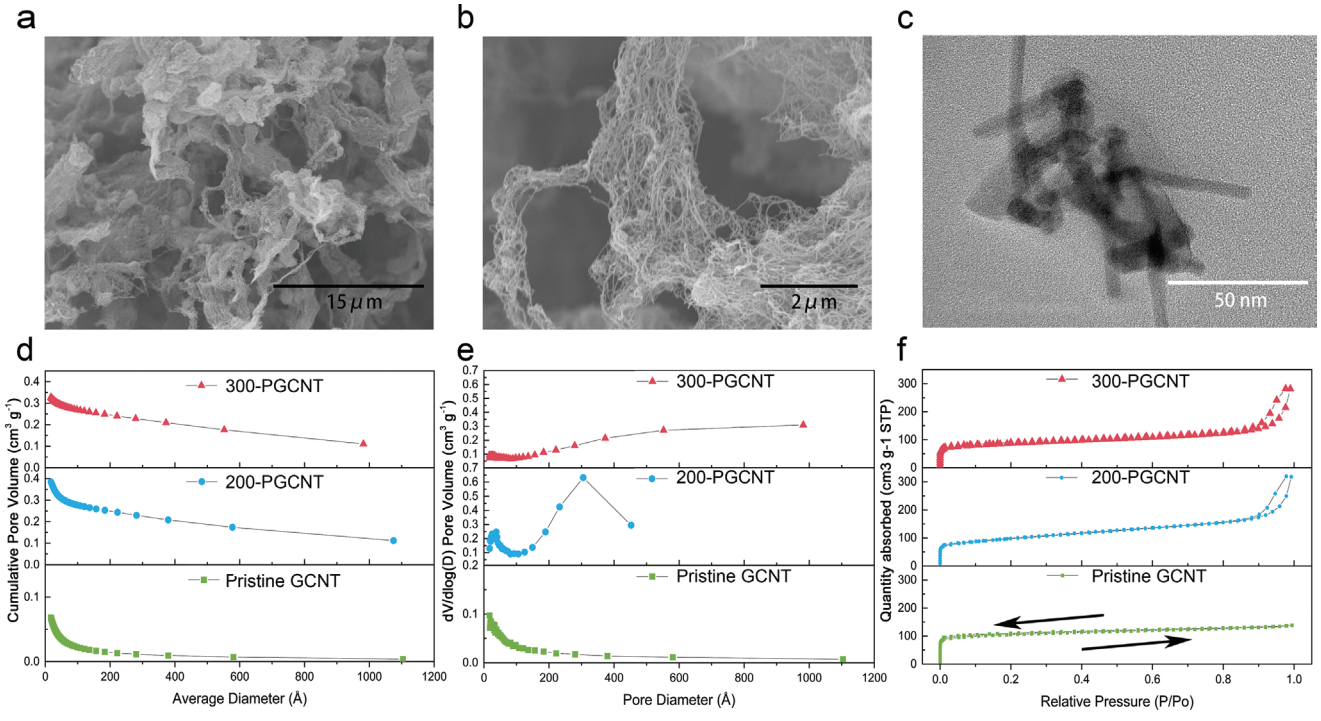

Figure 1. Scanning electron microscope (SEM) images of: a) 200-PGCNT and b) 300-PGCNT; c) transmission electron microscopy (TEM) image of 300-PGCNT, Brunauer–Emmett–Teller test (BET) testing result in: d) average diameter versus cumulative pore volume, e) pore diameter versus dV/dlog(D) pore volume, f) relative pressure versus quantity absorbed (cm^3 g^{-1} STP), the arrow pointing up is adsorption process and the other is adsorption process.

byproduct (carbon clusters). In Figure 1c, the transmission electron microscopy (TEM) image shows that the multiwalled CNTs has very uniform diameter, stacking up with each other to provide abundant pores and tunnels and the PGCNTs maintained the CNT structure after the P-atom doping.

Brunauer–Emmett–Telle (BET) measurement was conducted to evaluate the surface area and pore size distribution. The absorbate gas is nitrogen with an activation temperature of materials at 180 °C, which is followed by the absorption process at 77 K. The results of N_2 adsorption–desorption isotherms of pristine GCNT, 200 mg of NaH_2PO_2 reacted PGCNT (200-PGCNT), and 300 mg of NaH_2PO_2 reacted PGCNT (300-PGCNT) were shown in Figure 1d–f, which yielded a surface area of 333.7 $m^2\ g^{-1}$ for GCNT, 335.0 $m^2\ g^{-1}$ for 200-PGCNT, and 280.0 $m^2\ g^{-1}$ for 300-PGCNT. Further annealing in phosphurization process can result in a reduced surface area. There is a negligible difference in surface area between the pristine GCNT and 200-PGCNT, which implies the annealing of phosphurization with NaH_2PO_2 did not reduce the surface area of materials, however, the contribution of pores and defects changes the mesopores distribution. In Figure 1d, the pore volumes of 200-PGCNT and 300-PGCNT are much higher than that of pristine GCNT. Additionally, higher content of P-atom doping can result in an increased size of mesopores, which can provide larger tunnels for fast K^+ ion intercalation (Figure 1e). The pore diameter of pristine GCNT is mainly distributed ranging from 0 to 200 Å, while the pore diameter of 200-PGCNT shifted to a higher value ranging from 200 to 400 Å, where the peak is shown at around 300 Å (Figure 1e). Most of the pores have a diameter of 300-PGCNT distributed in the range over 400 Å and distributed evenly from 600 to 1000 Å. P-atom doping can not only provide lone pair electrons for absorption, but also increase the distance between the rigid CNTs to provide pores. Density functional theory (DFT) calculation has been done by Wang et al., and shows that the substitution of C atoms by P atoms gives a height of 78 Å between the protruding P and surface of CNTs.[40] Nevertheless, the pore size of the materials can affect ion transport in many ways. If the pore size is too low, it may slow down the cation migration; if the pore size is too high, it may not provide adequate structures to host cations.[41] The pore and pore size distribution should be controlled in suitable ranges, which can be achieved by phosphorization (annealing). According to the classification of the International Union of Pure and Applied Chemistry (IUPAC), three samples shown in Figure 1f were fitted according to Model I.[42] Type 1 model isothermal is a typical model for microporous materials. Three typical Langmuir isothermal model has a difference in the high P/P_0 area, where there are dramatic increases in 200-PGCNT and 300-PGCNT. The sharp increase at the end of the curve is attributed to the presence of voids among the particles which can occur similar to macroporous (50–7500 nm) adsorption.[43]

The X-ray photoelectron spectroscopy (XPS) is shown in **Figure 2**a, after the correction of the C spectra, there is no obvious peak found in spectra of P 2p in pristine GCNT, while there are two main peaks associated with P 2p in both phosphatized ones (Figure 2b,c), which means that the P atoms have been doped in the materials, although the amount of the doped P atoms and the mechanism of the doping is unclear. In the C 1s spectra (Figure 2d), the peaks at 284.6, 285.6, 290.5 eV represent C–C, C–O–C, and O–C=O, C=O bonds, respectively.[44] In the O 1s spectra (Figure 2f), the peaks at 532.1 and 534.0 eV represent C–O and C–O–H bond.[45] There is no obvious difference in those peaks compared to C 1s and O 1s from 300-PGCNT. This is due to the limited amount of doped phosphorous into the materials and the surface analysis nature of the XPS.

Raman spectra in Figure 2e show that the peak of the D band appears near 1350 cm^{-1} and the peak of G band appears near 1580 cm^{-1}. The D band contains disordered carbon atoms, and the G band is related to the graphitic hexagon-pinch mode.[46] Additionally, the broadened peak from 2500 to 3250 cm^{-1} can be divided into three peaks, which are accordingly referred to combination/overtone bands; 2659.8 cm^{-1} due to D+D band peak, 2950 cm^{-1} due to D + G band peak and 3160 cm^{-1} from G + G band peak. By comparing with the spectra of CNTs in the literature,[47,48] the Raman spectra further confirm the CNT has been maintained in the materials, with no obvious change in the peak shift. Additionally, Raman spectra can be utilized to analyze the defects within carbon materials. Because G-band presents the features of ordered pristine graphite while the D-band shows the disordered features of graphite sheet, the intensity ratio of the D-band to the G-band (I_D/I_G) can be used to compare the structural perfection.[47,49,50] After the simulation of the baseline to adjust it to zero and simulation of peaks, the value of the peak of G-band and D-band can be obtained. Both G-band and D-band of the CNTs are related to the motion of graphitic sp^2 carbon structures.[51] Although the position of the bands (D, G, D') in first-order Raman spectra presented very similar behavior in most cases, the intensity ratio of I_D/I_G can reflect the differences in their structure.[52] The G band peak in the spectra only disperse in more disordered carbon. And the degree of the disorderness is proportional to the intensity of the G band peak. Additionally, the strong D peak of carbon nanotube usually refers to its aligned structure.[52] In theory, the I_D/I_G ratio can be used to evaluate structural defects and the crystal domain size of the carbon materials.[53] Basically, the higher the intensity of the D-band, the larger the number of defects.[52] In conclusion, higher I_D/I_G ratio reflect higher defect concentrations. The intensity of D and G is represented by the area of each peak. After subtracting the baseline and fitting the peaks using a Gaussian model, the results are shown in Figure 1h. The I_D/I_G ratio of pristine GCNT, 200-PGCNT, and 300-PGCNT is 1.95, 2.79, and 2.94. The ratio of I_D/I_G shows an increased trend with P content which correlates with higher defect concentration.

X-ray diffraction (XRD) results have very strong background signal due to the presence of amorphous carbon (glucose) added into the materials, however, there is some information that can be compared among each material. As shown in Figure S11 (Supporting Information), the peaks around $2\theta = 27°$ and 43° refer to the (0 0 2) and (1 0 0) lattice planes of CNT.[54] The peaks of the 300-PGCNT is the most obvious and sharpest, while the peaks in GCNT is the widest, which means the more doped phosphorous, the better crystallinity the materials have.

The cyclic voltammetry (CV) test was conducted to confirm the potential range and the reaction kinetics. As shown in **Figure 3**a, the potential range of the cells range from 0.01 to 3.0 V and shows that most of the capacity is contributed from

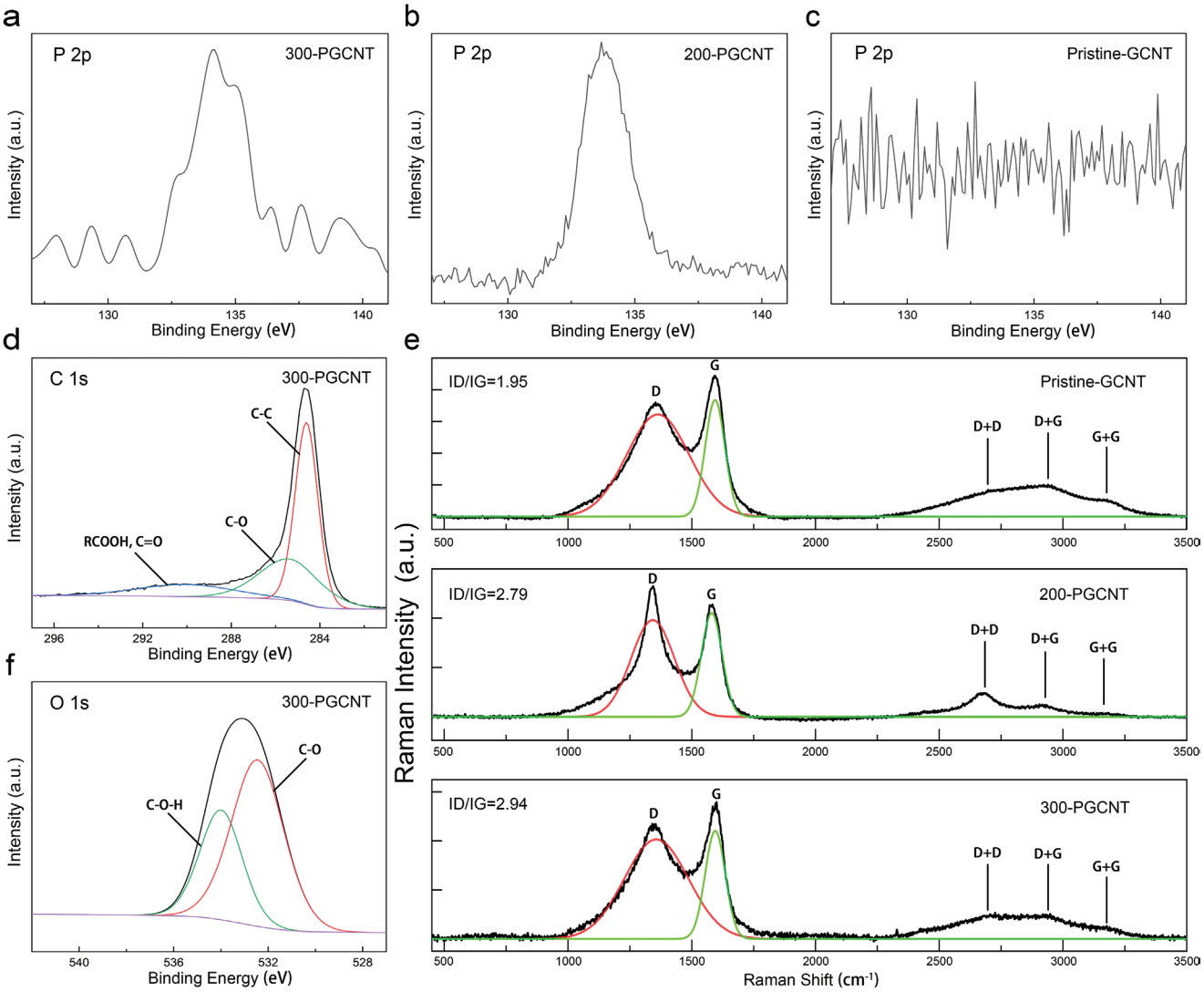

Figure 2. a–c) X-ray photoelectron spectroscopy (XPS) spectra of P 2p orbit of 300-PGCNT, 200PGCNT, Pristine-GCNT; d) XPS spectra of C 1s orbit of 300-PGCNT; e) Raman spectra of Pristine-GCNT, 200-PGCNT, and 300-PGCNT after baseline correction, I_D/I_G is the ratio of the intensity of *D* to the intensity of *G*; f) XPS spectra of O 1s orbit of 300-PGCNT.

0.01 to 2 V, however the batteries can maintain its reversibility when extending to 3 V. There are two symmetric peaks located at 1.1 and 0.3 V, which correspond to potassium ion deintercalation and intercalation. The difference between the first and the rest of CV cycles in Figure 3a is due to the creation of a solid electrolyte interface (SEI) film around 0.5 V (versus K/K^+), however, the loss of capacity caused by the SEI formation is confined to the first cycle, which can prove the formed SEI is stable. With the increase in the scan rate from 0.1 to 20 mV s^{-1}, the shape and the symmetry of the CV curve does not change. By analyzing the CV curve in Figure 3b, the GCNT dominant reaction can be recognized when compared with the CV curve of pristine GCNT in Figure S1 (Supporting Information).

GCD tests were undertaken at 0.1, 0.2, 0.5, 1, 2, 5 A g^{-1} current densities. As is shown in Figure 3c, doping P atoms into the materials can enhance the rate performance. The capacity retention under high current densities has a trend to increase with the increase of the P amount. The capacities of pristine GCNT, 200-PGCNT, and 300-PGCNT are about 20, 27, and 100 mAh g^{-1} at the current density of 5 A g^{-1}. The P atoms located in the carbon skeleton can provide anion defects host K^+ ion and facilitate the kinetics of K^+ ion transport,[55] which can increase the rate performance. Additionally, the CNT skeleton of the materials can protect the structure from collapse. Comparing 300-PGCNT with 200-PGCNT, we can conclude that a richer content of the P-atom doping helped enhance the rate performance. Additionally, the capacity of 300-PGCNT can reach 214 mAh g^{-1} at a current density of 0.1 A g^{-1} after 18 cycles (including 10 cycles of the activation). During the formation of P-atom doping, the charge from P transfers to GCNT, and the P-atoms can help the curved CNT skeleton to reduce its strain, which allow the carbon nanotube to accommodate phosphorus impurity, which also make the PGCNT an n-type semiconductor. This structural change only affects the first neighbors (carbon on CNTs structure) with only a small displacement for a second neighbor and negligible displacement for the third

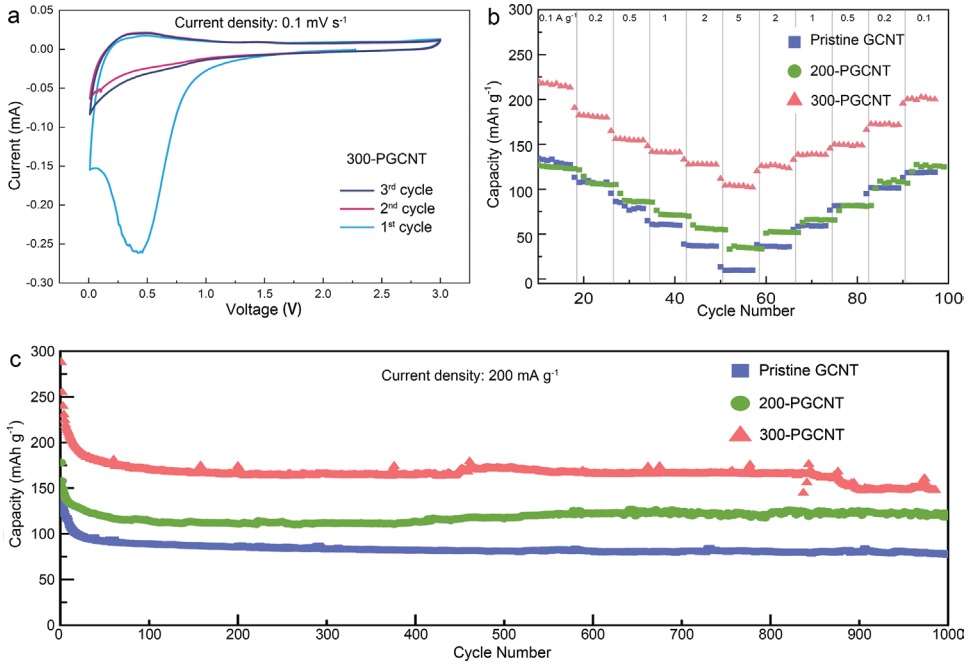

Figure 3. a) CV plots of 300-PGCNT at a scan rate of 0.1 mV s^{-1}; b) rate performance evaluation of pristine GCNT, 200-PGCNT and 300-PGCNT; c) long cycling stability measurement of pristine GCNT, 200-PGCNT, and 300-PGCNT at a current density of 200 mA g^{-1}.

nearest neighbor.[40] The electronic properties are enhanced by the P-atom doping which provides a new state inside the band structure. The band structure appears closer to the Fermi level compared with pristine GCNT, which means P doping can enhance the electronic conductivity which contributes to the high-rate performance. Additionally, because the substitution of C atom by P atom, each P atom is only surrounded by three neighboring carbon atoms, which means there is a lone pair of electrons for each inserted P atom. Based on above analysis, the mechanisms of K^+ ion storage consist of two parts: 1) K^+ ions intercalate and deintercalate into the carbon nanotube structure forming potassium carbides, where P-atom doping can form stable P–C bond preventing the collapse of materials structure and maintain its performance for long-term cycling. Also, the phosphorus doping can provide a fine pore size distribution (600–1000 Å) to facilitate fast, and large amount of K-ion storage; 2) the absorption of K^+ ion by lone pair electrons from doped P-atom can provide more active sites for hosting more K^+ ion, and hence store more energy.

Figure 3c compares the long-term cycling charge–discharge (CD) curves. The capacity of the batteries with different materials showed obvious decreases during the first few cycles due to the formation of stable SEI films, and, as is mentioned, the PIBs have relatively sluggish kinetics, PIBs require a few cycles for activation to achieve a stable and recyclable status. After that, the pristine G-CNT can reach 87 mAh g^{-1} at the 500th cycle and can still maintain the capacity of 80.4 mAh g^{-1} at the 950th cycle. After the phosphurization of GCNT, the capacity largely increases. After 500 cycles, 300-PGCNT maintained 170.7 mAh g^{-1} and 200-PGCNT maintained 116.6 mAh g^{-1}, further to the 950th cycle, 148.1 and 123.6 mAh g^{-1} were retained. The increased number of active sites and increased tunnels by adding P atoms can largely increase the capacity.

The Nyquist plot was utilized to demonstrate the results of impedance. In Figure S10 (Supporting Information), three plots are both structured by a half circle and a straight line, which means a combination of kinetic and diffusion resistance, where half circle represents the kinetic process, which consists of the resistance of solution and resistance of charge transfer (R_s + R_{ct}), and the straight line represents the diffusion-controlled process, which is also presented as Warburg resistance (Z_w). The diameter of the circle, representing the R_s + R_{ct} can be easily compared without fitting. The 300-PGCNT have the lowest kinetic resistance (R_s + R_{ct}) while the pristine GCNT have the highest value. The reason for the decreasing in kinetics is probably due to the increase amount of P atom doping. The impedance results further confirm the doping of P atom can lower down the internal resistance by changing the porosity distribution and providing more active sites. The much lower kinetic resistance can be main reasons of the enhanced rate compatibility.

CV profiles were conducted to study the charge storage mechanism and kinetics of the pristine GCNT (**Figure 4**a–c), 200-PGCNT (Figure S5 (Supporting Information)), and 300-PGCNT (Figure 4d–f) as anode materials for PIBs. The CV sequence curves of pristine GCNT, 200-PGCNT, and 300-PGCNT at different scan rates are shown in Figure S2 (Supporting Information).

The power-law formula is a relationship between current (i) and sweep rate (v) which can be used to study the kinetic process of K^+ ion storage: $i = av^b$, where a and b are extracted from the intercept and slope of equation: log i = $b$log v + log a.[16,56] When the b value equals to 0.5, ideal Faradaic intercalation process takes place which is controlled by semifinite linear diffusion. When b equals to 1, it is considered to be a capacitive response induced by surface charge.[57,58] In Figure 4b,

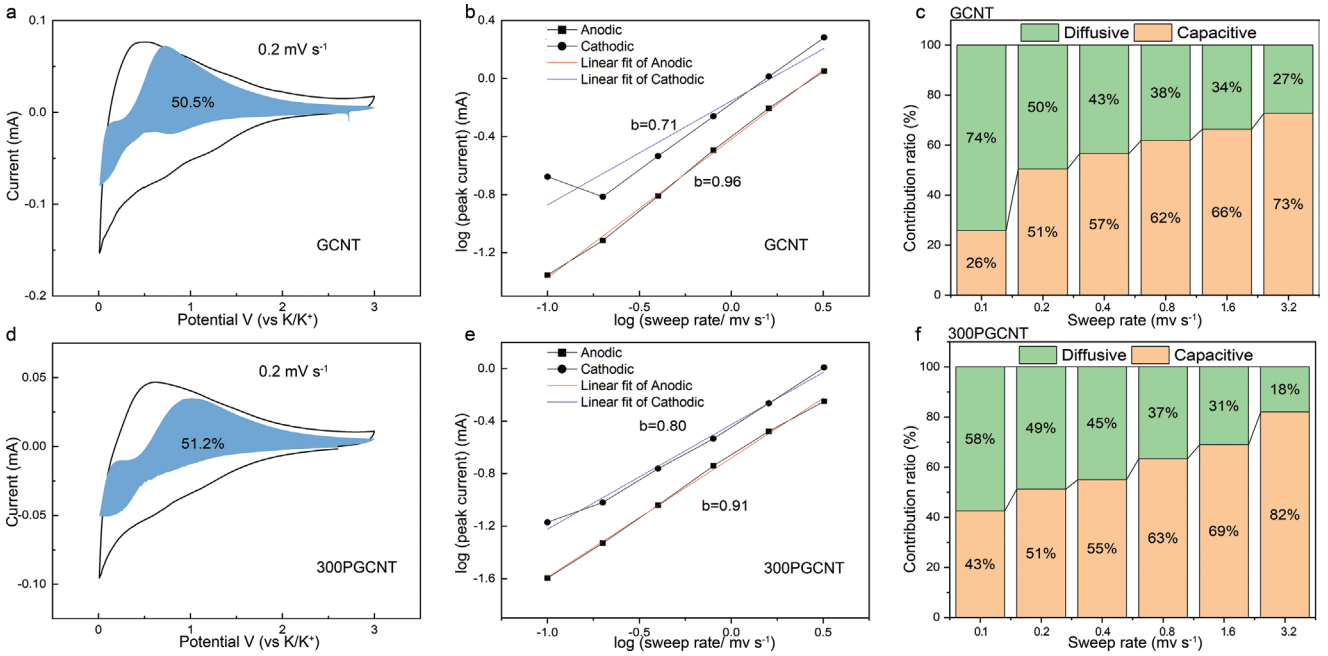

Figure 4. CV response (0.2 mV s^{-1}) for a) pristine GCNT and d) 300-PGCNT; relationships between log(*i*) and log(*V*) for b) pristine GCNT and e) 300-PGCNT; contributions of the capacitive and diffusion-controlled processes at different sweep rates for c) pristine GCNT and f) 300-PGCNT.

the *b* value of pristine GCNT calculated by the cathodic and anodic peaks are 0.71 and 0.96, which can imply the reaction process is most likely an equal combination of both capacitive and diffusion-controlled behaviors. The *b* values of cathodic and anodic peaks of 300-PGCNT are 0.80 and 0.91, respectively, which indicates it is a capacitive behavior dominant behavior with limited diffusion-controlled process. To further study the relative contribution of two mechanisms due to diffusive and capacitive reactions, the equation $i = k_1v + k_2v^{1/2}$ can be used, where i and v are current values under a given voltage and the scan rate of the test, respectively.[16] The equation can be further differentiated into $i/v^{1/2} = k_1v^{1/2} + k_2$, which can be used to model a linear fitting of $i/v^{1/2}$ versus $v^{1/2}$ to obtain the value of k_1 and k_2, factors that can be used to measure the proportion of the surface-controlled contribution and diffusion-controlled contribution.[58] Comparing Figure 4a,d, we learn that the capacitive contribution of the phosphorus containing one (300-PGCNT) (51.2%) is nearly equal to that of pristine GCNT (50.5%), which can also be confirmed from Figure 4c,f that the value of pristine GCNT gradually rises to 73% while the 300-PGCNT reaches 81% of capacitive contribution at a scan rate of 3.2 mV s^{-1} . The high capacitive distribution is also caused by the P-atom doping. As mentioned above, larger pore size distribution, higher electronic conductivity, and K^+ ion storage due to lone pair electrons of 300-PGCNT can promote the capacitive contribution.

3. Conclusion

In this work, GCNT backbone can provide good electrical conductivity and porosity for fast ion transport, but also provide a strong structure to facilitate the volume change during cycling. Additionally, phosphorus doping of GCNT has been shown to have a huge impact on the pore size distribution with negligible effect on the surface area. CNTs with suitable pore size distribution (600–1000 Å) were shown to have better rate performance and capacity than those with smaller pore size. The pore size can provide more tunnels and shorten pathway for K^+ ion transport, preventing the K^+ ion storage preferably take place on the outer shell of MWCNTs. PGCNT as an n-type semiconductor can provide higher electronic conductivity to facilitate the fast K^+ ion storage under high rates (104 mAh g^{-1} at current density of 5 A g^{-1}).

4. Experimental Section

Synthesis of Prisinte GCNT, 200-PGCNT, and 300-PGCNT: The synthesis of the materials including pristine GCNT, GCNTs doping with 200 mg P-source (200-GCNT) and GCNTs doping with 300 mg P-source (300-GCNT) were conducted by a one-step hydrothermal reaction followed by annealing. Firstly, MWCNTs and glucose were added into the lined vessel (100 mL PTFE) for hydrothermal reaction at 180 °C for 14 h. Secondly, the as-received samples were centrifuged (Thermo Scientific Sorvall ST 8) and freeze-dried to obtain the dried powder. Thirdly, the samples were annealed in a tube furnace (Carbolite MTF 12/38/400) at 700 °C in an argon atmosphere. The phosphorous doping was applied to the pristine GCNT sample. The pristine GCNT was then annealed with NaH_2PO_2 under an argon atmosphere at 350 °C for 2.5 h. An amount of 200 mg of NaH_2PO_2 and 300 mg of NaH_2PO_2 were added to react with 100 mg of prisine GCNT (200-GCNT, 300-GCNT) base-materials to produce materials with different ratios of dopant.

Fabrication of PGCNT Anode PIB Half-Cell: 200-PGCNT, 300-PGCNT, and pristine GCNT were mixed with carbon black (C65) and 10% PVDF/NMP in a weight ratio of 7:2:1 by Thinky mixer (Thinky, ARE-250) to form a homogeneous slurry, respectively. The slurry was then pasted

uniformly on a copper foil with ≈9 µm thickness by doctor blade and dried at 110 °C for 12 h in a vacuum oven. The dried electrode has been crimped into 16 mm discs prior to being assembled in a CR2032 coin cell with 16 mm potassium disc (99.9%, Sigma–Aldrich) as a counter electrode and microporous polyethene film as the separator in an argon-filled glovebox. The electrolyte used in this study was 1 M potassium bis(fluorosulfonyl)imide (KFSI) in the ethylene carbonate/diethyl carbonate (EC/DEC) with a weight ratio of 1:1.

Material Characterization: The morphologies of the composites were imaged by SEM (Joel JSM 6701 FEG-SEM) and TEM (JEOL, JEM-2100F). The surface area and porosity of the samples were evaluated by BET test (Micromeritics 3Flex surface characterization analyzer). The surface chemical environment of the composites was studied by XPS (Thermo-Scientific, K-alpha photoelectron spectrometer). The chemical information of the carbon was studied by Raman spectroscopy (DXR3 Raman Microscope, wavelength of 540 nm). The phase of the samples was identified by Cu source XRD (STOE SEIFERT).

Electrochemical Characterization: The working potential window and rate performance of the cells were determined by CV by a potentiostat (Biologic VSP 300). The rate performance and long-cycling performance were further studied by galvanostatic CD test using a Neware battery tester (Neware, BTS4000). Electrochemical impedance spectroscopy (EIS) tests were conducted with the frequency range of 10 kHz–10 mHz using a potentiostat (Biologic VSP 300).

Supporting Information

Supporting Information is available from the Wiley Online Library or from the author.

Acknowledgements

The authors acknowledge the Engineering and Physical Sciences Research Council (EPSRC, EP/V027433/1, EP/V027433/2).

Conflict of Interest

The authors declare no conflict of interest.

Data Availability Statement

The data that support the findings of this study are available from the corresponding author upon reasonable request.

Keywords

anodes, carbon materials, high-rate, potassium-ion batteries

Received: October 25, 2022
Revised: November 19, 2022
Published online:

[1] R. Rajagopalan, Y. Tang, X. Ji, C. Jia, H. Wang, R. Rajagopalan, Y. Tang, X. Ji, H. Wang, C. Jia, *Adv. Funct. Mater.* **2020**, *30*, 1909486.
[2] S. Ren, Y. Hao, L. Xu, H. Wu, N. Ba, *Energy Econ.* **2021**, *98*, 105220.
[3] T. Ahmad, D. Zhang, *Energy Rep.* **2020**, *6*, 1973.
[4] W. Zhang, J. Mao, S. Li, Z. Chen, Z. Guo, *J. Am. Chem. Soc.* **2017**, *139*, 3316.
[5] Y. Liu, Z. Tai, J. Zhang, W. K. Pang, Q. Zhang, H. Feng, K. Konstantinov, Z. Guo, H. K. Liu, *Nat. Commun.* **2018**, *9*, 3645.
[6] Y. Liu, C. Yang, Q. Pan, Y. Li, G. Wang, X. Ou, F. Zheng, X. Xiong, M. Liu, Q. Zhang, *J. Mater. Chem. A* **2018**, *6*, 15162.
[7] J. Yang, Z. Ju, Y. Jiang, Z. Xing, B. Xi, J. Feng, S. Xiong, J. L. Yang, Z. C. Ju, Z. Xing, Y. Jiang, B. J. Xi, S. L. Xiong, J. K. Feng, *Adv. Mater.* **2018**, *30*, 1700104.
[8] J. Qin, H. M. Kheimeh Sari, C. He, X. Li, *J. Mater. Chem. A* **2019**, *7*, 3673.
[9] F. Xu, Y. Zhai, E. Zhang, Q. Liu, G. Jiang, X. Xu, Y. Qiu, X. Liu, H. Wang, S. Kaskel, *Angew. Chem., Int. Ed.* **2020**, *59*, 19460.
[10] W. Zhang, Z. Cao, W. Wang, E. Alhajji, A.-H. Emwas, P. M. F. J. Costa, L. Cavallo, H. N. Alshareef, *Angew. Chem., Int. Ed.* **2020**, *59*, 4448.
[11] B. Wang, Z. Zhang, F. Yuan, D. Zhang, Q. Wang, W. Li, Z. Li, Y. A. Wu, W. Wang, *Chem. Eng. J.* **2022**, *428*, 131093.
[12] X. Shi, Y. Zhang, G. Xu, S. Guo, A. Pan, J. Zhou, S. Liang, *Sci. Bull.* **2020**, *65*, 2014.
[13] P. Luo, C. Zheng, J. He, X. Tu, W. Sun, H. Pan, Y. Zhou, X. Rui, B. Zhang, K. Huang, *Adv. Funct. Mater.* **2021**, *32*, 2107277.
[14] H. Ding, J. Zhou, A. M. Rao, B. Lu, *Natl. Sci. Rev.* **2021**, *8*, nwaa276.
[15] Y. Chen, L. Qin, Y. Lei, X. Li, J. Dong, D. Zhai, B. Li, F. Kang, *ACS Appl. Mater. Interfaces* **2019**, *11*, 45578.
[16] S. Chong, S. Qiao, X. Wei, T. Li, L. Yuan, S. Dong, W. Huang, *iScience* **2021**, *24*, 103494.
[17] L. Fang, J. Xu, S. Sun, B. Lin, Q. Guo, D. Luo, H. Xia, *Small* **2019**, *15*, 1804806.
[18] S. Chong, X. Wei, Y. Wu, L. Sun, C. Shu, Q. Lu, Y. Hu, G. Cao, W. Huang, *ACS Appl. Mater. Interfaces* **2021**, *13*, 13158.
[19] W. Zong, H. Guo, Y. Ouyang, L. Mo, C. Zhou, G. Chao, J. Hofkens, Y. Xu, W. Wang, Y.-E. Miao, G. He, I. P. Parkin, F. Lai, T. Liu, *Adv. Funct. Mater.* **2022**, *32*, 2110016.
[20] S. Zhao, Z. Guo, K. Yan, X. Guo, S. Wan, F. He, B. Sun, G. Wang, *Small Struct.* **2021**, *2*, 2000054.
[21] X. Chen, H. Zhang, C. Ci, W. Sun, Y. Wang, *ACS Nano* **2019**, *13*, 3600.
[22] S. Tian, Y. Wang, T. Cai, D. Kong, D. Wang, H. Ren, W. Xing, *Appl. Surf. Sci.* **2020**, *534*, 147635.
[23] X. Chen, H. Muheiyati, X. Sun, P. Zhou, P. Wang, X. Ding, Y. Qian, L. Xu, *Small* **2022**, *18*, 2104363.
[24] D. Liu, X. Huang, D. Qu, D. Zheng, G. Wang, J. Harris, J. Si, T. Ding, J. Chen, D. Qu, *Nano Energy* **2018**, *52*, 1.
[25] S. Xiong, Y. Jiang, W. Liang, S. Deng, Y. Wang, S. Luan, R. Chen, L. Hou, Z. Zhang, F. Gao, *ChemElectroChem* **2021**, *8*, 3767.
[26] G. Chen, J. Chen, I. P. Parkin, G. He, T. S. Miller, *ChemElectroChem* **2022**, *9*, 202200800.
[27] S. Liu, J. Mao, L. Zhang, W. Kong Pang, A. Du, Z. Guo, *Adv. Mater.* **2021**, *33*, 2006313.
[28] M. Gu, L. Fan, J. Zhou, A. Rao, B. Lu, *ACS Nano* **2021**, *15*, 9167.
[29] L. Fan, R. Ma, Q. Zhang, X. Jia, B. Lu, *Angew. Chem., Int. Ed.* **2019**, *58*, 10500.
[30] L. Qin, N. Xiao, J. Zheng, Y. Lei, D. Zhai, Y. Wu, *Adv. Energy Mater.* **2019**, *9*, 1902618.
[31] Q. Liu, A. M. Rao, X. Han, B. Lu, *Adv. Sci.* **2021**, *8*, 2003639.
[32] X. Wu, Y. Chen, Z. Xing, C. W. K. Lam, S.-S. Pang, W. Zhang, Z. Ju, *Adv. Energy Mater.* **2019**, *9*, 1900343.
[33] X. Shi, Z. Xu, C. Han, R. Shi, X. Wu, B. Lu, J. Zhou, S. Liang, *Nano-Micro Lett.* **2020**, *13*, 21.
[34] W. Yang, J. Zhang, D. Huo, S. Sun, S. Tao, Z. Wang, J. Wang, D. Wu, B. Qian, *Ionics* **2019**, *25*, 4795.
[35] G. Lu, H. Wang, Y. Zheng, H. Zhang, Y. Yang, J. Shi, M. Huang, W. Liu, *Electrochim. Acta* **2019**, *319*, 541.
[36] K. Lei, C. Wang, L. Liu, Y. Luo, C. Mu, F. Li, J. Chen, *Angew. Chem., Int. Ed.* **2018**, *57*, 4687.
[37] P. G. Bruce, B. Scrosati, J. M. Tarascon, *Angew. Chem., Int. Ed.* **2008**, *47*, 2930.

[38] J. Bai, B. Xi, H. Mao, Y. Lin, X. Ma, J. Feng, S. Xiong, J. Bai, B. J. Xi, H. Z. Mao, X. J. Ma, S. L. Xiong, Y. Lin, J. K. Feng, *Adv. Mater.* **2018**, *30*, 1802310.
[39] Z. Jian, W. Luo, X. Ji, *J. Am. Chem. Soc.* **2015**, *137*, 11566.
[40] H. M. Wang, H. X. Wang, Y. Chen, Y. J. Liu, J. X. Zhao, Q. H. Cai, X. Z. Wang, *Appl. Surf. Sci.* **2013**, *273*, 302.
[41] D. Wang, J. Jiang, Z. Pan, Q. Li, J. Zhu, L. Tian, P. K. Shen, *Front. Mater.* **2019**, *6*, 245.
[42] H. Swenson, N. P. Stadie, *Langmuir* **2019**, *35*, 5409.
[43] F. Ambroz, T. J. Macdonald, V. Martis, I. P. Parkin, *Small Methods* **2018**, *2*, 1800173.
[44] Y. Bourlier, M. Bouttemy, O. Patard, P. Gamarra, S. Piotrowicz, J. Vigneron, R. Aubry, S. Delage, A. Etcheberry, *ECS J. Solid State Sci. Technol.* **2018**, *7*, P329.
[45] S. Yang, Y. Liu, Y. Hao, X. Yang, W. A. Goddard, X. L. Zhang, B. Cao, *Adv. Sci.* **2018**, *5*, 1700659.
[46] L. P. Yuan, Z. Y. Wu, W. J. Jiang, T. Tang, S. Niu, J. S. Hu, *Nano Res.* **2020**, *13*, 1376.
[47] S. Yoon, S. Lee, S. Kim, K. W. Park, D. Cho, Y. Jeong, *J. Power Sources* **2015**, *279*, 495.
[48] M. S. Dresselhaus, G. Dresselhaus, R. Saito, A. Jorio, *Phys. Rep.* **2005**, *409*, 47.
[49] C. Thomsen, S. Reich, *Phys. Rev. Lett.* **2000**, *85*, 5214.
[50] R. Saito, A. Jorio, J. H. Hafner, C. M. Lieber, M. Hunter, T. McClure, G. Dresselhaus, M. S. Dresselhaus, *Phys. Rev. B* **2001**, *64*, 085312.
[51] G. A. Zickler, B. Smarsly, N. Gierlinger, H. Peterlik, O. Paris, *Carbon* **2006**, *44*, 3239.
[52] E. F. Antunes, A. O. Lobo, E. J. Corat, V. J. Trava-Airoldi, A. A. Martin, C. Veríssimo, *Carbon* **2006**, *44*, 2202.
[53] R. J. Nemanich, S. A. Solin, *Phys. Rev. B* **1979**, *20*, 392.
[54] A. Cao, C. Xu, J. Liang, D. Wu, B. Wei, *Chem. Phys. Lett.* **2001**, *344*, 13.
[55] X. Lu, X. Zhang, Y. Zheng, D. Zhang, L. Jiang, F. Gao, Q. Liu, D. Fu, J. Teng, W. Yang, *Proc. Natl. Acad. Sci.* **2022**, *119*, e2122252119.
[56] V. Augustyn, J. Come, M. A. Lowe, J. W. Kim, P. L. Taberna, S. H. Tolbert, H. D. Abruña, P. Simon, B. Dunn, *Nat. Mater.* **2013**, *12*, 518.
[57] S. Zeng, X. Zhou, B. Wang, Y. Feng, R. Xu, H. Zhang, S. Peng, Y. Yu, *J. Mater. Chem. A* **2019**, *7*, 15774.
[58] J. Wang, J. Polleux, J. Lim, B. Dunn, *J. Phys. Chem. C* **2007**, *111*, 14925.